RSC Advances

PAPER

View Article Online
View Journal | View Issue

Cite this: *RSC Adv.*, 2014, **4**, 44302

Preparation of magnetic mesoporous core–shell nanocomposites for cinnamic acid hydrogenation†

Xiaofang Liu, Lingjuan Shi, Wenhui Feng, Libo Niu, Chen Liu and Guoyi Bai*

Received 16th July 2014
Accepted 11th September 2014

DOI: 10.1039/c4ra07176j

www.rsc.org/advances

A novel magnetic mesoporous core–shell nanocomposite Fe_3O_4@nSiO_2@mSiO_2@Ni–Co–B was prepared by the combination of a modified Stöber sol–gel process, a surfactant-templating method and self-assembly. It has a multi-shell structure with ferroferric oxide as core, dense nonporous silica and mesoporous silica as middle layers in sequence and an Ni–Co–B amorphous alloy as outer layer, as confirmed by transmission electron microscopy and nitrogen adsorption–desorption. This nanocomposite showed high activity and good selectivity in the selective hydrogenation of cinnamic acid to hydrocinnamic acid. Notably, it can be easily separated by a magnet after reaction due to its high magnetism and recycled effectively five times.

1. Introduction

In recent years, magnetic core–shell silica nanocomposites, which combine the functionalities of magnetic cores and silica shells, have attracted much attention not only due to their unique structures but also their wide applications in the fields of drug delivery, catalysis, environment protection, bioseparation and so on.[1–7] For example, Lin *et al.* have prepared a multifunctional Fe_3O_4@nSiO_2@mSiO_2@YVO_4:Eu^{3+} composite material, which possesses ordered hexagonal mesopores, bright luminescence, high magnetization saturation value, and can be potentially used as targeted drug delivery system.[4] Zhao *et al.* have prepared Fe_3O_4@SiO_2–Au@mSiO_2 microspheres, which showed high conversion and selectivity in the catalytic reduction of 4-nitrophenol and styrene epoxidation.[5] Zhang *et al.* have designed an effective Fe_3O_4@SiO_2@mSiO_2–Pd(0) catalyst for Suzuki coupling reaction.[6] However, most of these catalysts applied noble metals as active components, and the high price of noble metals limited their further applications.

On the other hand, Ni–B amorphous alloy catalysts have attracted much interest in hydrogenation reactions owing to their unique isotropic nature, high concentration of coordinative unsaturated sites, and low cost.[8–12] However, most of the pure Ni–B amorphous alloys showed either poor stability or activity. Thus, great efforts have been attempted to solve these problems. For example, Liu *et al.* have reported a supported Ni–B/boehmite catalyst, which exhibited good activity and stability in the hydrogenation of *p*-nitrophenol and *p*-chloronitrobenzene.[9] Recently, we have prepared a Fe_3O_4@nSiO_2@Ni–La–B core–shell catalyst and obtained good results in the hydrogenation of benzophenone.[10] However, due to its low surface area, large amounts of active components and catalyst were applied in that reaction. Thus, there is still a need to develop a more efficient catalyst with higher surface area and lower active components loadings. Mesoporous materials, which have high surface area and large pore volume, can facilitate the loading of the active components and might be a good choice to solve this problem.

Very recently, we have prepared a NiCoB/γ-Al_2O_3-u catalyst, which showed both suitable activity and stability in *tert*-butanol, in the selective hydrogenation of cinnamic acid to hydrocinnamic acid,[11] an important chemical intermediate.[13,14] But the used catalyst was separated by leaching for recycling, not as effective as magnetic separation. Combined with the results of our previous work[10–12] and the structural benefit of mesoporous materials, we designed a novel Fe_3O_4@nSiO_2@mSiO_2@Ni–Co–B (n: nonporous, m: mesoporous) magnetic mesoporous nanocomposite with four layer core–shell structure and evaluated it in the selective hydrogenation of cinnamic acid to hydrocinnamic acid. As envisaged, Fe_3O_4@nSiO_2@mSiO_2@Ni–Co–B showed high activity, good selectivity and stability under relatively mild reaction conditions. Meanwhile, it can be easily separated from the reaction mixture by magnet and effectively recycled.

2. Experimental

2.1. Preparation of catalysts

Unless otherwise stated, all chemicals were purchased from Baoding Huaxin Reagent and Apparatus Co., Ltd. and were used as received without further purification. The Fe_3O_4@nSiO_2@mSiO_2@Ni–Co–B nanocomposite was prepared by a multistep procedure, as shown in Scheme 1. Fe_3O_4@nSiO_2@mSiO_2 was

Key Laboratory of Medicinal Chemistry and Molecular Diagnosis of Ministry of Education, College of Chemistry and Environmental Science, Hebei University, Baoding 071002, P.R. China. E-mail: baiguoyi@hotmail.com; Fax: +86-312-5937102; Tel: +86-312-5079359

† Electronic supplementary information (ESI) available. See DOI: 10.1039/c4ra07176j

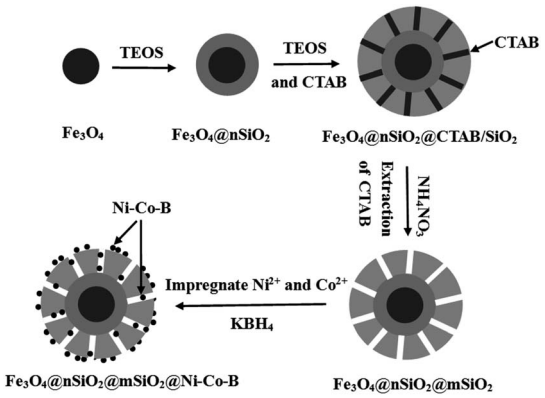

Scheme 1 Preparation of Fe_3O_4@$nSiO_2$@$mSiO_2$@Ni–Co–B.

first prepared according to the method similar to the literature[15] (for details, see the ESI†). Then, 0.5 g Fe_3O_4@$nSiO_2$@$mSiO_2$ was impregnated with an aqueous solution of $NiCl_2 \cdot 6H_2O$ (0.506 g) and $CoCl_2 \cdot 6H_2O$ (0.051 g) (molar ratio Ni : Co = 10 : 1). After drying at 313 K, the precursor was reduced by adding 8.6 mL of 1.0 M aqueous KBH_4 containing 0.2 M NaOH dropwise in an ice water bath under ultrasound. After the reduction was finished, the precipitate was first separated using magnet and then washed with deionized water several times until neutral, followed by washing with absolute ethanol three times to remove the residual water. Finally, the obtained Fe_3O_4@$nSiO_2$@$mSiO_2$@Ni–Co–B nanocomposite was kept under absolute ethanol for further use. Fe_3O_4@$nSiO_2$@Ni–Co–B, Ni–Co–B, and Ni–Co–B/$mSiO_2$ were prepared in a similar manner to the protocol reported in our previous work.[10–12]

2.2. Catalyst characterization

X-ray diffraction (XRD) patterns were obtained on a Bruker D8 diffractometer using a Cu Kα radiation source. The Fourier transform infrared spectra (FT-IR) were tested on a Bruker VERTEX 70 Fourier transform spectrophotometer using KBr pellets. Transmission electron microscopy (TEM), selected-area electron diffraction (SAED) and X-ray energy dispersive spectroscopy (EDS) were carried out on a microscope JEM-2100F instrument. BET surface area and pore volume of the nanocomposites were measured using a Micromeritics Tristar II 3020 surface area and pore analyzer. Magnetization curves were performed on a LDJ9600-1 Superconducting quantum interference device at room temperature.

2.3. Activity test

Selective hydrogenation of cinnamic acid (Scheme 2) was performed as follows: cinnamic acid (3.0 g), catalyst (0.1 g) and *tert*-butanol (200 mL) were mixed in a 500 mL stainless steel autoclave equipped with a mechanical stirrer and electric heating system. The autoclave was filled with H_2 three times to exclude residual air and then pressurized to 3.0 MPa with H_2. After it was heated to 373 K, hydrogenation was started by stirring the reaction mixture vigorously and allowed to proceed for 1 h. Reaction mixtures were analyzed by gas chromatography using

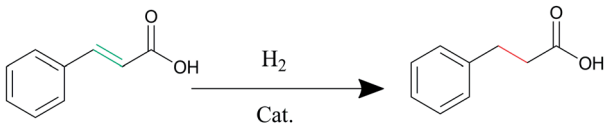

Scheme 2 Selective hydrogenation of cinnamic acid.

a 30 m SE-30 capillary column and the product structures were identified using gas chromatography-mass spectrometry (GC-MS) on an Agilent 5975C spectrometer. The used catalyst was separated by magnet, washed with *tert*-butanol and then kept under *tert*-butanol for recycling.

3. Results and discussion

Fig. 1A shows the wide-angle XRD patterns of Fe_3O_4, Fe_3O_4@$nSiO_2$@$mSiO_2$, Fe_3O_4@$nSiO_2$@$mSiO_2$@Ni–Co–B, and Fe_3O_4@$nSiO_2$@Ni–Co–B. The characteristic diffraction peaks of these magnetic core–shell nanocomposites are just like those of pure Fe_3O_4, which possess a face-centered cubic structural (*Fd3m* space group) magnetite (JCPDS no. 19-0629), indicating that the magnetic cores were well retained after the silica coating.[16] Furthermore, the broad band at 2θ = 20–30° in Fe_3O_4@$nSiO_2$@$mSiO_2$, Fe_3O_4@$nSiO_2$@$mSiO_2$@Ni–Co–B, and Fe_3O_4@$nSiO_2$@Ni–Co–B can be assigned to the amorphous

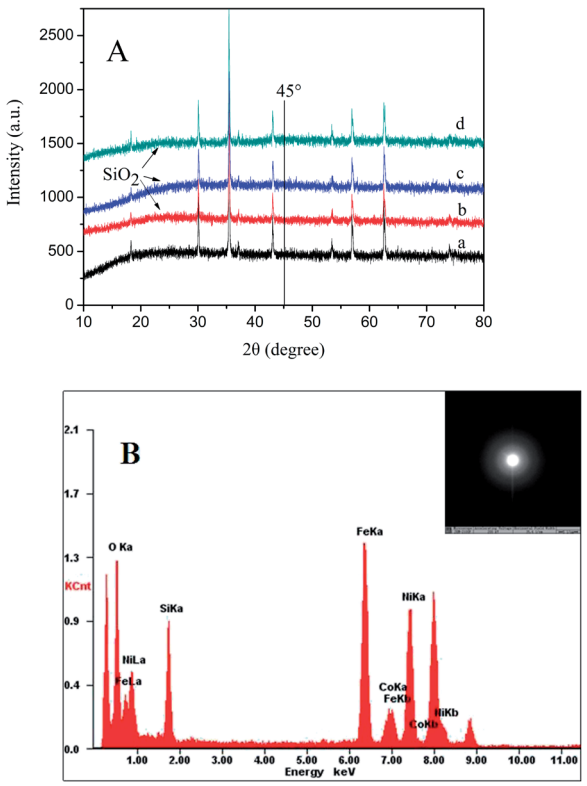

Fig. 1 (A) Wide-angle XRD patterns of (a) Fe_3O_4, (b) Fe_3O_4@$nSiO_2$@$mSiO_2$, (c) Fe_3O_4@$nSiO_2$@$mSiO_2$@Ni–Co–B and (d) Fe_3O_4@$nSiO_2$@Ni–Co–B; (B) EDS spectrum of Fe_3O_4@$nSiO_2$@$mSiO_2$@Ni–Co–B (inset of B : SAED image).

SiO_2, suggesting that both the $nSiO_2$ and $mSiO_2$ shells existed in an amorphous state.[4] In contrast, no characteristic diffraction peaks related to Ni–Co–B amorphous alloy can be observed at about $2\theta = 45°$ in Fe_3O_4@$nSiO_2$@Ni–Co–B and Fe_3O_4@$nSiO_2$@$mSiO_2$@Ni–Co–B. Fortunately, both Ni and Co can be detected by EDS on the surface of Fe_3O_4@$nSiO_2$@$mSiO_2$@Ni–Co–B (Fig. 1B) and its amorphous structure can be further confirmed by a successive diffraction halo in the SAED image (Fig. 1B inset).[17] Thus, the amorphous Ni–Co–B was suggested to be well dispersed on the surface of the $mSiO_2$ shell.

FT-IR spectra of Fe_3O_4@$nSiO_2$@CTAB/SiO_2 without the treatment of ethanol containing NH_4NO_3 and the obtained Fe_3O_4@$nSiO_2$@$mSiO_2$ nanocomposites are presented in Fig. 2. The adsorption peak appearing at about 571 cm^{-1} is assigned to the characteristic absorption peak of Fe–O bond, indicating the presence of Fe_3O_4 magnetic nanaoparticles. The absorption peaks at 1075 cm^{-1} and 792 cm^{-1}, 945 cm^{-1}, 457 cm^{-1} correspond to Si–O–Si, Si–OH, Si–O respectively, demonstrating the formation of SiO_2.[18] For the Fe_3O_4@$nSiO_2$@CTAB/SiO_2, the bands observed in the region of 2800–3000 cm^{-1} are attributed to the vibrations of $-CH_2$ of CTAB templates. In contrast, no adsorption peaks were observed in the range of 2800–3000 cm^{-1} for the Fe_3O_4@$nSiO_2$@$mSiO_2$ nanocomposites, suggesting that the CTAB templates have been completely removed after the treatment with ethanol containing NH_4NO_3.[16]

The low-angle XRD patterns of Fe_3O_4@$nSiO_2$@$mSiO_2$ and Fe_3O_4@$nSiO_2$@$mSiO_2$@Ni–Co–B are shown in Fig. 3. The sole diffraction peak at about $2\theta = 2°$ for both the samples indicated the long-range ordered structures of them. Considering the high similarity of these two low-angle XRD patterns, we could suggest that the uniform mesoporous structures were maintained after loading of Ni–Co–B.[19]

TEM images of Fe_3O_4@$nSiO_2$@$mSiO_2$ and Fe_3O_4@$nSiO_2$@$mSiO_2$@Ni–Co–B are exhibited in Fig. 4. As can be seen, Fe_3O_4@$nSiO_2$@$mSiO_2$ nanocomposite exhibits a clear multi-shell structure with a magnetite core, a nonporous silica shell in the middle, and a mesoporous silica shell outside (Fig. 4a), although certain aggregation occurred due to the inherent magnetism of magnetite. The magnetite core is approximately

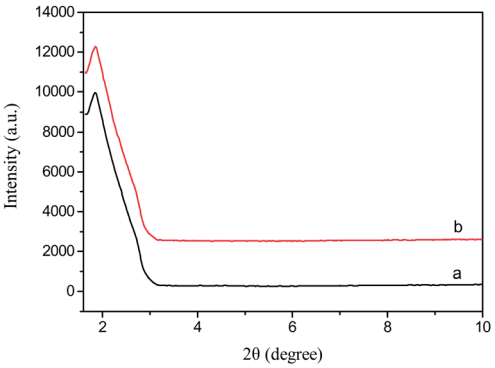

Fig. 3 Low-angle XRD patterns of (a) Fe_3O_4@$nSiO_2$@$mSiO_2$ and (b) Fe_3O_4@$nSiO_2$@$mSiO_2$@Ni–Co–B.

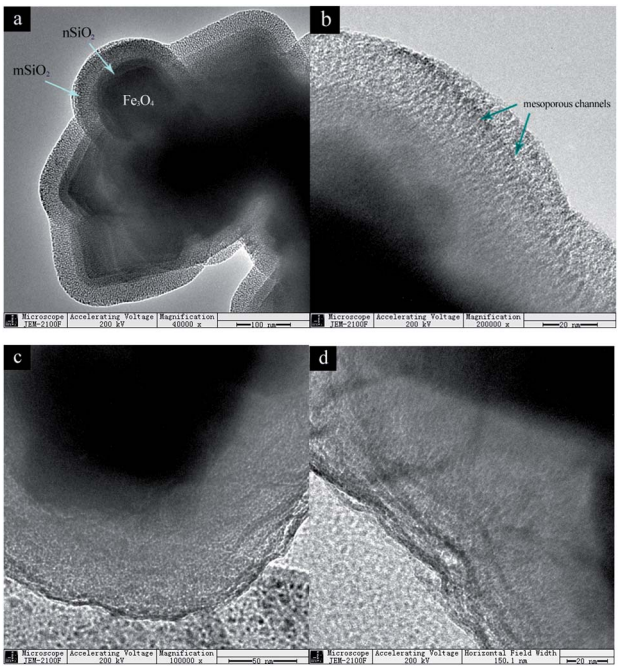

Fig. 4 TEM images of (a and b) Fe_3O_4@$nSiO_2$@$mSiO_2$ and (c and d) Fe_3O_4@$nSiO_2$@$mSiO_2$@Ni–Co–B.

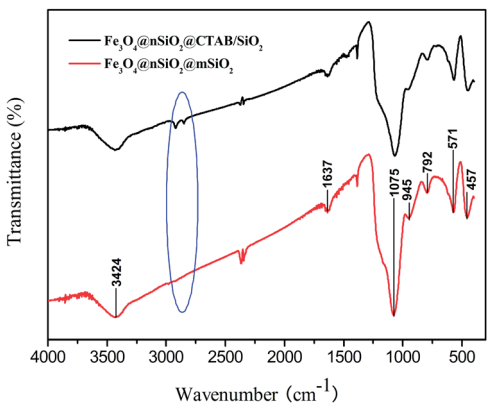

Fig. 2 FT-IR spectra of Fe_3O_4@$nSiO_2$@CTAB/SiO_2 and Fe_3O_4@$nSiO_2$@$mSiO_2$.

100 nm in diameter, the inner nonporous silica shell is approximately 20 nm and the mesoporous silica shell is approximately 45 nm with some mesoporous channels (as indicated by the arrows in Fig. 4b). In contrast, Fe_3O_4@$nSiO_2$@$mSiO_2$@Ni–Co–B keeps a typical multi-shell structure (Fig. 4c and d), but not as clear as Fe_3O_4@$nSiO_2$@$mSiO_2$ after the loading of Ni–Co–B, implying the Ni–Co–B amorphous alloy being dispersed on the outer surface or in the pores of $mSiO_2$.

Fig. 5 exhibits the nitrogen adsorption–desorption isotherms and pore size distribution curves of Fe_3O_4@$nSiO_2$@$mSiO_2$, Fe_3O_4@$nSiO_2$@$mSiO_2$@Ni–Co–B and Fe_3O_4@$nSiO_2$@Ni–Co–B. The nitrogen sorption isotherms of Fe_3O_4@$nSiO_2$@$mSiO_2$ resembled a reversible IV-type isotherm[20] with nearly no hysteresis loop (Fig. 5A(a)), mainly due to the reversible pore filling in the P/P_0 range of 0.2–0.4 as a form of capillary condensation.[21] In contrast, Fe_3O_4@$nSiO_2$@$mSiO_2$@Ni–Co–B

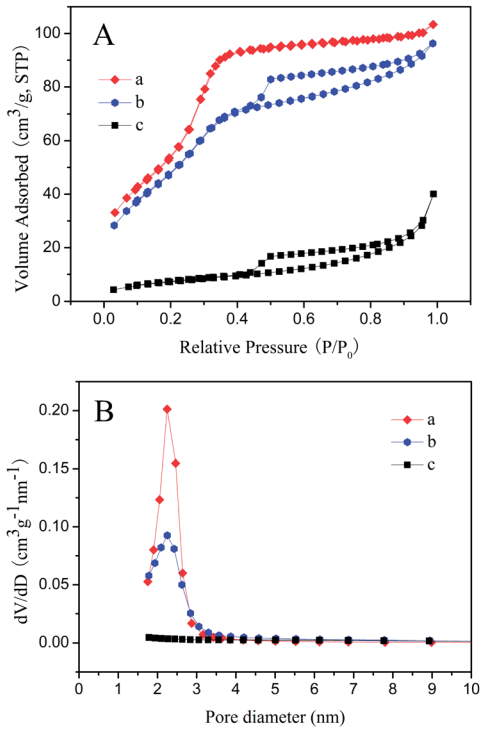

Fig. 5 (A) N_2 adsorption–desorption isotherms and (B) pore size distribution curves of (a) Fe_3O_4@nSiO_2@mSiO_2, (b) Fe_3O_4@nSiO_2@mSiO_2@Ni–Co–B and (c) Fe_3O_4@nSiO_2@Ni–Co–B.

exhibited a IV-type isotherm with an obvious hysteresis loop, which is likely to be associated with some interstitial structures form among the aggregated particles in the sample.[22] Their pore size distribution curves (Fig. 5B(a) and (b)) presented a sharp peak at about 2.3 nm, which verified their mesoporous structure.[23] In contrast, the nitrogen sorption isotherms of Fe_3O_4@nSiO_2@Ni–Co–B showed III-type isotherm[24] (Fig. 5A(c)) and its pore size distribution curve merely fluctuated slightly over a wide range (Fig. 5B(c)), indicating its nearly non-porous structure.

The results of BET surface area and pore volume of the core–shell nanocomposites and Ni–Co–B are summarized in Table 1. It was found that the surface area markedly increased from 5.1 to 302.8 $m^2\ g^{-1}$ and the pore volume from 0.009 to 0.186 $cm^3\ g^{-1}$ after coating an mSiO_2 shell outside of Fe_3O_4@nSiO_2, also demonstrating the mesoporous structure of Fe_3O_4@nSiO_2@mSiO_2. Considering that the BET surface area and pore volume of Fe_3O_4@nSiO_2@mSiO_2@Ni–Co–B decreased to 200.0 $m^2\ g^{-1}$ and 0.145 $cm^3\ g^{-1}$ respectively, we speculated that Ni–Co–B has dispersed on the outer surface and occupied some pores of Fe_3O_4@nSiO_2@mSiO_2.[25] However, these values of Fe_3O_4@nSiO_2@mSiO_2@Ni–Co–B are still much higher than those of Fe_3O_4@nSiO_2@Ni–Co–B, ascribed to the presence of mSiO_2.

The room temperature hysteresis loops of Fe_3O_4@nSiO_2@mSiO_2@Ni–Co–B nanocomposite and Ni–Co–B amorphous alloy at an applied field of 60 000 Oe are shown in Fig. 6. As can be seen, the saturation magnetization (M_s) value is 8.83 emu g^{-1} for Fe_3O_4@nSiO_2@mSiO_2@Ni–Co–B and no remanence or hysteresis loops are detectable, indicating its super-paramagnetism;[26] whereas, the Ms value of Ni–Co–B is only 0.08 emu g^{-1}. Obviously, due to its high Ms value, Fe_3O_4@nSiO_2@mSiO_2@Ni–Co–B can be easily separated for recycling by an external magnetic field; but the pure Ni–Co–B cannot (Fig. 6 inset).

The catalytic performance of the two core–shell nanocomposites were tested in the hydrogenation of cinnamic acid and Ni–Co–B was also evaluated for comparison, and the results are listed in Table 1. As can be seen, the conversion of cinnamic acid was 100% over Fe_3O_4@nSiO_2@mSiO_2@Ni–Co–B, much higher than those of Fe_3O_4@nSiO_2@Ni–Co–B (58.4%) and Ni–Co–B (65.9%), although the selectivity for hydrocinnamic acid were 100% for all catalysts. We ascribed this to the effect of

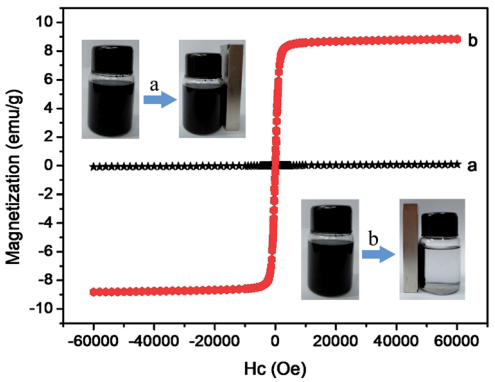

Fig. 6 Room temperature hysteresis loops of (a) Ni–Co–B, (b) Fe_3O_4@nSiO_2@mSiO_2@Ni–Co–B, and the inset is the magnetic separation process of (a) Ni–Co–B, (b) Fe_3O_4@nSiO_2@mSiO_2@Ni–Co–B by a magnet within 40 seconds.

Table 1 Structural properties and catalytic performance of the core–shell nanocomposites and Ni–Co–B[a]

Sample	BET surface area ($m^2\ g^{-1}$)	Pore volume ($cm^3\ g^{-1}$)	Conversion (%)	Selectivity (%)
Fe_3O_4@nSiO_2	5.1	0.009	—	—
Fe_3O_4@nSiO_2@mSiO_2	302.8	0.186	—	—
Fe_3O_4@nSiO_2@Ni–Co–B	27.0	0.062	58.4	100.0
Fe_3O_4@nSiO_2@mSiO_2@Ni–Co–B	200.0	0.145	100.0	100.0
Ni–Co–B[b]	21.9	0.064	65.9	100.0

[a] Reaction conditions: 3.0 g cinnamic acid, 0.1 g catalyst (20 wt% Ni–Co–B), 200 mL *tert*-butanol, temperature at 373 K, initial $P(H_2) = 3.0$ MPa, and reaction time 1 h. [b] Ni–Co–B 0.02 g.

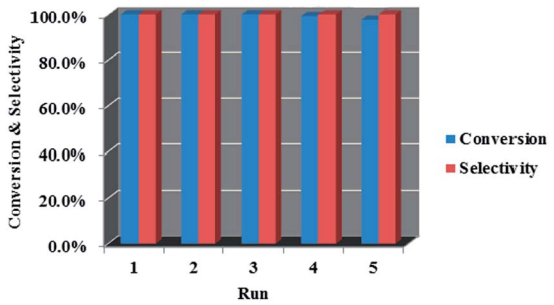

Fig. 7 Reusability studies of Fe_3O_4@$nSiO_2$@$mSiO_2$@Ni–Co–B on the selective hydrogenation of cinnamic acid to hydrocinnamic acid. Reaction conditions: 3.0 g cinnamic acid, 0.1 g catalyst (20 wt% Ni–Co–B), 200 mL *tert*-butanol, temperature at 373 K, initial $P(H_2)$ = 3.0 MPa, and reaction time 1 h.

the $mSiO_2$ shell, which can not only benefit the self-assembly of Ni–Co–B by modulating the surface negatively charged,[27] but also promote the dispersion of Ni–Co–B nanoparticle on its mesoporous surface. The good catalytic performance of Ni–Co–B/$mSiO_2$ can support this assumption, which also shows 100% conversion and selectivity in the hydrogenation of cinnamic acid. However, it must be separated by centrifugation, which is not as convenient as magnetic separation of Fe_3O_4@$nSiO_2$@$mSiO_2$@Ni–Co–B. Furthermore, we think the low BET surface area (5.1 $m^2\ g^{-1}$) and pore volume (0.009 $cm^3\ g^{-1}$) of Fe_3O_4@$nSiO_2$ should account for the lower activity of Fe_3O_4@$nSiO_2$@Ni–Co–B, compared to Ni–Co–B. Finally, the stability of Fe_3O_4@$nSiO_2$@$mSiO_2$@Ni–Co–B was investigated in the hydrogenation of cinnamic acid and the results were depicted in Fig. 7. As expected, this core–shell nanocomposite can be easily separated by magnet and recycled five times without significant loss of its initial catalytic activity with the selectivity for hydrocinnamic acid still keeping 100%.

4. Conclusions

In conclusion, a novel magnetic mesoporous core–shell nanocomposite Fe_3O_4@$nSiO_2$@$mSiO_2$@Ni–Co–B was prepared and showed excellent activity in the selective hydrogenation of cinnamic acid to hydrocinnamic acid. The existence of the $mSiO_2$ shell affords this nanocomposite larger surface area and pore volume, making the active Ni–Co–B species highly dispersed on its surface, and then accounting for its high activity. Meanwhile, this nanocomposite can be easily separated by magnet after reaction due to its high magnetism and recycled five times without significant loss of its initial catalytic activity, demonstrating its good stability.

Acknowledgements

Financial support by the National Natural Science Foundation of China (21376060), the Natural Science Foundation of Hebei Province (B2014201024), and the Science Foundation of Hebei University (3333112) are gratefully acknowledged.

Notes and references

1 Z. H. Xu, C. X. Li, X. J. Kang, D. M. Yang, P. P. Yang, Z. Y. Hou and J. Lin, *J. Phys. Chem. C*, 2010, **114**, 16343–16350.
2 J. P. Ge, Q. Zhang, T. R. Zhang and Y. D. Yin, *Angew. Chem., Int. Ed.*, 2008, **47**, 8924–8928.
3 D. G. He, X. X. He, K. M. Wang, Y. X. Zhao and Z. Zou, *Langmuir*, 2013, **29**, 5896–5904.
4 P. P. Yang, Z. W. Quan, Z. Y. Hou, C. X. Li, X. J. Kang, Z. Y. Cheng and J. Lin, *Biomaterials*, 2009, **30**, 4786–4795.
5 Y. H. Deng, Y. Cai, Z. K. Sun, J. Liu, C. Liu, J. Wei, W. Li, C. Liu, Y. Wang and D. Y. Zhao, *J. Am. Chem. Soc.*, 2010, **132**, 8466–8473.
6 W. Li, B. L. Zhang, X. J. Li, H. P. Zhang and Q. Y. Zhang, *Appl. Catal., A*, 2013, **459**, 65–72.
7 H. M. Chen, S. S. Liu, H. L. Yang, Y. Mao, C. H. Deng, X. M. Zhang and P. Y. Yang, *Proteomics*, 2010, **10**, 930–939.
8 J. B. Zheng, Z. Q. Xia, J. J. Li, W. K. Lai, X. D. Yi, B. H. Chen, W. P. Fang and H. L. Wan, *Catal. Commun.*, 2012, **21**, 18–21.
9 H. Liu, J. Deng and W. Li, *Catal. Lett.*, 2010, **137**, 261–266.
10 G. Y. Bai, L. J. Shi, Z. Zhao, Y. L. Wang, M. D. Qiu and H. X. Dong, *Mater. Lett.*, 2013, **96**, 93–96.
11 G. Y. Bai, H. X. Dong, Z. Zhao, H. L. Chu, X. Wen, C. Liu and F. Li, *RSC Adv.*, 2014, **4**, 19800–19805.
12 G. Y. Bai, H. X. Dong, Z. Zhao, Y. L. Wang, Q. Z. Chen and M. D. Qiu, *J. Nanosci. Nanotechnol.*, 2013, **13**, 5012–5016.
13 K. Lan and Z. X. Shan, *Synth. Commun.*, 2007, **37**, 2171–2177.
14 K. J. P. Narayana, P. Prabhakar, M. Vijayalakshmi, Y. Venkateswarlu and P. S. J. Krishna, *Pol. J. Microbiol.*, 2007, **56**, 191–197.
15 Y. H. Deng, D. W. Qi, C. H. Deng, X. M. Zhang and D. Y. Zhao, *J. Am. Chem. Soc.*, 2008, **130**, 28–29.
16 C. Wang, S. Y. Tao, W. Wei, C. G. Meng, F. Y. Liu and M. Han, *J. Mater. Chem.*, 2010, **20**, 4635–4641.
17 H. Li, J. Liu, H. X. Yang and H. Li, *J. Mater. Res.*, 2009, **24**, 3300–3307.
18 S. Z. Li, Y. Ma, X. L. Yue, Z. Cao and Z. F. Dai, *New J. Chem.*, 2009, **33**, 2414–2418.
19 X. H. Zhu, Y. Z. Chen, F. W. Zhang, J. R. Niu, M. Xie and J. T. Ma, *RSC Adv.*, 2014, **4**, 2509–2514.
20 J. P. Yang, F. Zhang, Y. R. Chen, S. Qian, P. Hu, W. Li, Y. H. Deng, Y. Fang, L. Han, M. Luqmanb and D. Y. Zhao, *Chem. Commun.*, 2011, **47**, 11618–11620.
21 P. J. Branton, K. Kaneko and N. Setoyama, *Langmuir*, 1996, **12**, 599–600.
22 S. S. Liu, H. M. Chen, X. H. Lu, C. H. Deng, X. M. Zhang and P. Y. Yang, *Angew. Chem., Int. Ed.*, 2010, **49**, 7557–7561.
23 Z. N. Liu, H. H. Yang, H. Zhang, C. J. Huang and L. F. Li, *Cryogenics*, 2012, **52**, 699–703.
24 H. F. Liu, S. F. Ji, H. Yang, H. Zhang and M. Tang, *Ultrason. Sonochem.*, 2014, **21**, 505–512.
25 R. Xu, G. Y. Sun, Q. Y. Li, E. B. Wang and J. M. Gu, *Solid State Sci.*, 2010, **12**, 1720–1725.
26 X. H. Zhang and L. Jiang, *J. Mater. Chem.*, 2011, **21**, 10653–10657.
27 D. W. Wang, X. M. Zhu, S. F. Lee, H. M. Chan, H. W. Li, S. K. Kong, J. C. Yu, C. H. K. Cheng, Y. X. J. Wang and K. C. F. Leung, *J. Mater. Chem. B*, 2013, **1**, 2934–2942.